AGU PUBLICATIONS

JGR

Journal of Geophysical Research: Biogeosciences

RESEARCH ARTICLE
10.1002/2014JG002824

T. Hwang, L. E. Band, and T. C. Hales contributed equally to the paper.

Key Points:
- Lidar remote sensing is effective in estimating spatial root cohesion patterns
- Belowground vegetation information improves slope stability prediction

Supporting Information:
- Supporting Information S1

Correspondence to:
T. Hwang,
taehee@indiana.edu

Citation:
Hwang, T., L. E. Band, T. C. Hales, C. F. Miniat, J. M. Vose, P. V. Bolstad, B. Miles, and K. Price (2015), Simulating vegetation controls on hurricane-induced shallow landslides with a distributed ecohydrological model, *J. Geophys. Res. Biogeosci.*, *120*, 361–378, doi:10.1002/2014JG002824.

Received 14 OCT 2014
Accepted 28 JAN 2015
Accepted article online 1 FEB 2015
Published online 27 FEB 2015

Simulating vegetation controls on hurricane-induced shallow landslides with a distributed ecohydrological model

Taehee Hwang[1,2], Lawrence E. Band[1,3], T. C. Hales[4], Chelcy F. Miniat[5], James M. Vose[6], Paul V. Bolstad[7], Brian Miles[2], and Katie Price[8]

[1]Institute for the Environment, University of North Carolina at Chapel Hill, Chapel Hill, North Carolina, USA, [2]Now at Department of Geography, Indiana University Bloomington, Bloomington, Indiana, USA, [3]Department of Geography, University of North Carolina at Chapel Hill, Chapel Hill, North Carolina, USA, [4]School of Earth and Ocean Sciences, Cardiff University, Cardiff, UK, [5]Coweeta Hydrologic Laboratory, USDA Forest Service, Otto, North Carolina, USA, [6]Southern Research Station, USDA Forest Service, Raleigh, North Carolina, USA, [7]Department of Forest Resources, University of Minnesota, Saint Paul, Minnesota, USA, [8]Department of Geosciences, Georgia State University, Atlanta, Georgia, USA

Abstract The spatial distribution of shallow landslides in steep forested mountains is strongly controlled by aboveground and belowground biomass, including the distribution of root cohesion. While remote sensing of aboveground canopy properties is relatively advanced, estimating the spatial distribution of root cohesion at the forest landscape scale remains challenging. We utilize canopy height information estimated using lidar (light detecting and ranging) technology as a tool to produce a spatially distributed root cohesion model for landslide hazard prediction. We characterize spatial patterns of total belowground biomass based on the empirically derived allometric relationship developed from soil pit measurements in the Coweeta Hydrologic Laboratory, North Carolina. The vertical distribution of roots and tensile strength were sampled at soil pits allowing us to directly relate canopy height to root cohesion and use this model within a distributed ecohydrological modeling framework, providing transient estimates of runoff, subsurface flow, soil moisture, and pore pressures. We tested our model in mountainous southern Appalachian catchments that experienced a number of landslides during the 2004 hurricane season. Slope stability estimates under the assumption of spatially uniform root cohesion significantly underpredicted both the total number of landslides and the number of "false positives," unfailed areas of the landscape that were predicted to fail. When we incorporate spatially distributed root cohesion, the accuracy of the slope stability forecast improves dramatically. With the growing availability of lidar data that can be used to infer belowground information, these methods may provide a wider utility for improving landslide hazard prediction and forecasting.

1. Introduction

Landslides are significant geophysical hazards in steep mountainous areas. Shallow landslides act as an important mechanism of transfer of hillslope sediment to channels [*Benda and Dunne*, 1997] and an ecologic disturbance mechanism [*White*, 1979]. The initiation of shallow landslides depends on the interactions between soil physical properties, hillslope hydrology, and belowground ecologic processes [*Wu*, 1995]. On steep slopes, plant roots increase soil shear strength, particularly in the low-cohesion colluvial soils where shallow landslides initiate [*Hales et al.*, 2009; *Roering et al.*, 2003]. Rooting structures also have a strong control on long-term hillslope hydrology, imparting high soil hydraulic conductivity and macroporosity typically resulting in negligible infiltration excess runoff generation, such that drainage is dominated by shallow to deep subsurface flow. In the short-term, vegetation moderates pore pressures by reducing antecedent soil moisture through transpiration and interception and facilitating drainage by increasing macropore flow. The combined hydrologic and soil stabilizing effects of vegetation increase slope stability on mountainous watersheds [*Ghestem et al.*, 2011]. Therefore, understanding the spatial and temporal patterns of root contributions to soil strength combined with hydrological modeling of pore pressure will improve regional landslide hazard assessment and forecasting [*Band et al.*, 2012].

There are three predominant approaches taken for landslide hazard prediction, depending on available data and spatial scale of the analysis. The first method, typically applied at a reconnaissance or regional scale, is a topographically based application of an infinite slope equation with a simple hillslope hydrology model

which provides estimates of slope stability [e.g., *Montgomery and Dietrich*, 1994]. A second method is event-specific forecasting for a regional scale, applied using sophisticated geotechnical models that take into account antecedent conditions and short-term precipitation forecasting or real-time estimation [e.g., *Chen and Lee*, 2003]. A third method uses multiple regressions of climate, streamflow, and other hydrological variables to create rule-based models of landslide initiation potential [e.g., *Berti et al*., 2012]. The first method often assumes worst-case scenarios of probable maximum precipitation or specific low frequency storms, while the second requires assessment of specific transient events, for which warnings can be developed. The third approach requires long records of landslides, climate, and hydrological information before implementation. For transient event forecasting, additional critical needs are the contributions of ecosystem water use on local hydrology, particularly during interstorm periods that condition antecedent soil saturation levels, local topography, and estimates of soil hydraulics and strength characteristics, including the contributions of roots to soil strength.

Physically based, regional landslide hazard models, such as Shallow Landsliding Stability Model (SHALSTAB) and Stability Index Mapping (SINMAP), often assume steady state flow conditions at specific rainfall or recharge rates [e.g., *Montgomery and Dietrich*, 1994; *Pack et al*., 2005]. However, in the southern Appalachians, as elsewhere, slope failures are often associated with heavy, short-term precipitation events predominantly from subtropical storm systems in late summer and early fall [*Fuhrmann et al*., 2008; *Wooten et al*., 2007] and are significantly influenced by antecedent conditions, violating the steady state assumption. The sequence and timing of large storms is an important determinant of landslide occurrence, with closely spaced or long duration events providing greater spatial frequency of landslides due to spatial heterogeneity of soil saturation. The combination of intense precipitation, wet antecedent conditions, and convergent topography promotes high pore pressures that can result in transient decreases in soil strength sufficient to initiate a mass failure [*Band et al*., 2012; *Lehmann and Or*, 2012].

The main challenge of regional landslide forecasting is the uncertainty associated with the spatial distribution of the physical parameters, primarily cohesion, friction angle, and soil depth. Despite significant advances in hydrologic and topographic modeling, our understanding of the distribution of root and soil properties remains poor. Soil strength (friction and cohesion) can be parameterized using soil maps, but the spatial precision of soil map information is typically low compared to the resolution of digital elevation data [*Zhu et al*., 1997]. The net effect of these assumptions often translates into spatially uniform classifications of hazard zones, from which landslide hazard becomes dependent on topography-derived slope and drainage area, as well as precipitation patterns. In steep terrain with colluvial soils (such as Macon County, NC), roots often provide a primary source of spatial variability in slope reinforcement. Friction angles occupy a relatively narrow range of values in this region (vary between 33° and 38°), but root cohesion (C_r) can vary by an order of magnitude depending on the vegetation community types occurring at a particular slope [*Hales et al*., 2009].

Root cohesion is a function of the number and distribution of roots within a soil column and their elastic properties. Vertical root distributions often depend on vegetation community types [*Schenk and Jackson*, 2002] and the long-term distribution of soil moisture in a landscape [*Hales et al*., 2009]. Regional controls on root elastic properties are not well understood, however. Root tensile properties are therefore implicitly assumed to be static through the storm events that initiate landslides, although the strength of soil-root bond may vary with moisture [*Pollen-Bankhead and Simon*, 2009]. Recently, *Hales et al*. [2013] found that root strength varies strongly with root moisture content; roots are weakest at full saturation and strongest when dry. Hence, a regional root reinforcement model must account for the role of community type, rooting depth and biomass, and feedbacks between root moisture state and soil hydrology. However, there have been few studies to characterize regional-scale root cohesion patterns in space and time for improving landslide hazard prediction and mapping.

Remotely sensed vegetation information could be an important tool for developing spatial models of root reinforcement for landslide mapping or forecasting [*Miller*, 2013]. Currently remote sensing is used to detect the postevent distributions of landslides [*Glade*, 2003; *Miller*, 2013; *Montgomery et al*., 2000], using spectral vegetation indices (e.g., normalized difference vegetation index (NDVI)) or vegetation cover using land cover classification. We contend that this application could be extended to improve potential landslide forecasts. Forest ecosystems have predictable patterns of foliar and root biomass in response to available water and nutrient resources along hydrologic flow paths [*Hwang et al*., 2009]. General patterns of belowground biomass can be estimated along these flow paths as aboveground and belowground biomass pools are

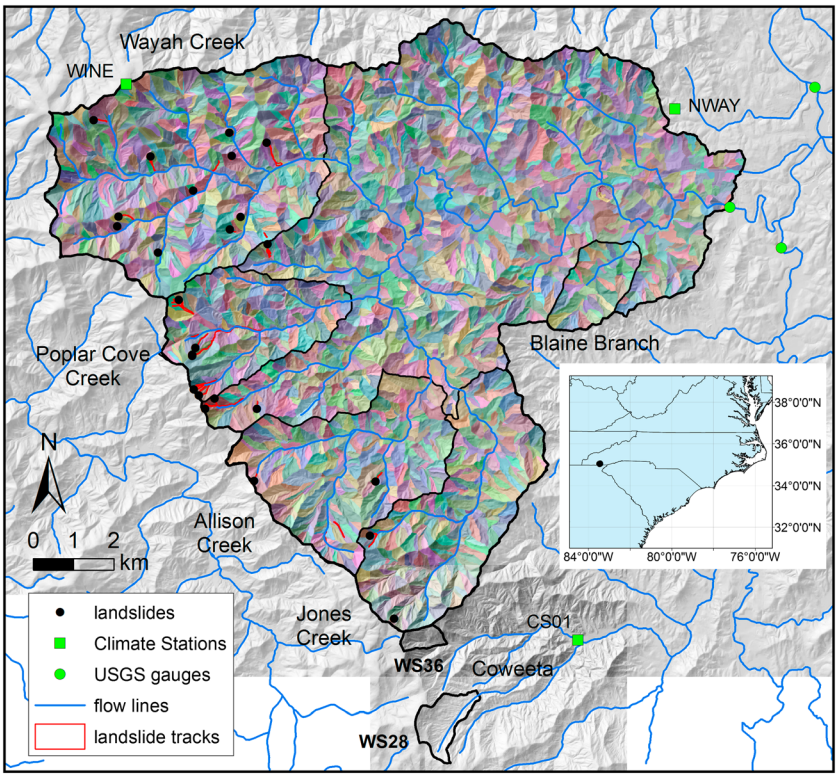

Figure 1. The Cartoogechaye watershed in the Little Tennessee River, five gauged subwatersheds (Wayah Creek, Poplar Cove Creek, Allison Creek, Jones Creek, and Blaine Branch; Table 1), and subcatchments ($n = 1388$, with different colors) used in the evaluation process. Green points represent the climate stations (WINE, NWAY, and CS01; Table 3) and USGS gauge stations (Cartoogechaye Creek near Franklin, NC; ID 03500240). Black circles indicate observed landslide initiation locations during the two consecutive hurricane events in 2004 from North Carolina Geological Survey (http://portal.ncdenr.org/web/lr/geological_home). Coweeta Hydrologic Lab is located in the southeast of the study site.

often related, expressed as an allometric or a root-to-shoot ratio [*Litton et al.*, 2007]. While aboveground biomass and other canopy structural properties can be estimated using lidar (light detecting and ranging) technology [*Lee and Lucas*, 2007; *Lefsky et al.*, 2002, 2005; *Popescu and Wynne*, 2004; *Popescu et al.*, 2003; *Song et al.*, 2010], estimating belowground biomass is more challenging. However, the combination of empirical allometric relationships with lidar canopy data represents a significant improvement in our ability to derive estimates of root biomass across the landscape and therefore the root contribution to soil strength.

In this paper, we explore the coupling of a distributed ecohydrological model incorporating existing spatial patterns of canopy conditions, topography, and soils with a planar landslide model. Our work builds on previous observations of the spatial variability in root strength characteristics between overstory hardwood forest and shrub species in the southern Appalachians [*Hales et al.*, 2009] and simple planar landslide models driven by a distributed ecohydrologic model [*Band et al.*, 2012]. We hypothesize that the use of spatially variable root cohesion patterns, estimated from aboveground properties, will improve the simulation of landslide risk at the storm event scale. Our main research questions are the following: (1) Can canopy height information derived from lidar data be used to estimate and map the spatial distribution of root properties and soil cohesive strength using simple allometric relations? (2) How effective is the incorporation of spatially variable root properties, including root biomass and cohesion, on improving the prediction skill of landslide occurrence in small subcatchments during major hurricane events in the southern Appalachians?

2. Methods and Materials

2.1. Study Site

The study site is the Cartoogechaye Creek watershed, located in western North Carolina in the Little Tennessee River basin (Figure 1), which experienced significant landslide activity during two closely spaced hurricanes in

Table 1. Gauged Subwatersheds in the Study Site and Land Use and Land Cover Information[a]

Subwatershed	Area (km^2)	Developed (%)	Forest/Shrub (%)	Pasture/Agriculture (%)
Wayah Creek	30.6	2.9	96.7	0.3
Poplar Cove Creek	9.6	8.5	90.1	1.4
Allison Creek	15.2	6.1	90.4	3.4
Jones Creek	15.3	3.3	94.3	2.4
Blaine Branch	3.3	8.4	82.3	9.1

[a]From National Land Cover Database (NLCD) 2006 [*Price et al.*, 2011].

2004 (Frances and Ivan). The study site is typical of southern Appalachian forests, with dominant mixed hardwood forests including *Quercus* spp. (oaks), *Carya* spp. (hickory), *Nyssa sylvatica* (black gum), *Betula lenta* (black birch), *Acer rubrum* (red maple), and *Liriodendron tulipifera* (tulip poplar). Major evergreen understory species are *Rhododendron maximum* (rhododendron) and *Kalmia latifolia* (mountain laurel) [*Day et al.*, 1988]. *Tsuga canadensis* (eastern hemlock) has been a common evergreen overstory species on riparian and mesic sites but has now been significantly reduced by an invasive insect (hemlock woolly adelgid) since early 2004 [*Ford and Vose*, 2007; *Ford et al.*, 2012]. Soils are of colluvial origin on steep hillsides with broadleaf forest cover, with the exception of alluvial soils in the floodplains of the larger valleys that are typically cleared for pasture, agriculture, or development [*Hales et al.*, 2009]. Roads in steeper, forested areas have been significantly extended with new second home development in the last two decades. Mean annual precipitation in the area from low to high elevation ranges from 1800 to 2500 mm [*Laseter et al.*, 2012]. Precipitation is relatively evenly distributed through the year, although tropical storms in late summer and early fall can deliver high storm totals and intensities. Stream discharge records for the Cartoogechaye Creek watershed are available from USGS

Table 2. Site Characteristics and Belowground Biomass Values of Soil Pits

Watershed	Species	Topographic Position	Basal Area Map[a] or DBH (cm)	Measured Belowground Biomass ($g\ m^{-2}$)	Estimated Belowground Biomass ($g\ m^{-2}$)
WS28	*Liriodendron tulipifera*	Hollow	H1	1440.8	1288.5
		Hollow	H2	2896.7	3978.7
		Hollow	H3	1970.0	1494.2
		Nose	N1	5240.5	4338.5
		Nose	N2	2365.8	2395.9
		Nose	N3	1054.7	
	Betula lenta	Hollow	H1	1739.7	1088.0
		Hollow	H2	1070.5	695.4
		Hollow	H3	1017.0	743.8
		Nose	N1	1293.5	
		Nose	N2	1171.9	743.8
		Nose	N3	1495.3	
WS36	*Acer saccharum*	Nose	20.9		1156.7
	Tsuga canadensis	Nose	33.9		314.9
	Rhododendron maximum	Hollow	4.3		604.4
	Carya spp.	Nose	38.8		1032.4
	L. tulipifera	Side Slope	17.5		462.9
	Quercus rubra	Hollow	84.0		700.4
	A. rubrum	Nose	5.1		373.9
	Q. prinus	Nose	58.7		2093.2
	Q. velutina	Hollow	33.7		526.1
	Q. rubra	Hollow	37.7		614.3
	Q. rubra	Nose	33.2		1068.5
	R. maximum	Nose	9.2		339.8
	B. lenta	Hollow	28.5		1600.1
	L. tulipifera	Hollow	22.5		923.5
	L. tulipifera	Nose	20.1		598.6

[a]Basal area maps are available in Figure S2.

gauge in Franklin (ID 03500240) since 1961. Streamflow from a set of five subwatersheds within the Cartoogechaye Creek watershed was available for 2007–2009 (Table 1 and Figure 1) [*Price et al.*, 2011].

The area has been the site of repeated debris flows. The 2004 hurricane season resulted in a number of debris flows initiating in steep, high-elevation areas, typically at the head of hillslope hollows in areas with subtle topographic convergence [*Wooten et al.*, 2007]. A series of larger slope failures were documented and mapped in the headwaters of the study site by the North Carolina Geological Survey (http://portal.ncdenr.org/web/lr/landslides-information; Figure 1).

2.2. Belowground Biomass Measurements

Belowground biomass was measured directly by weighing roots or estimated by measuring the cross-sectional area of all roots and adjusting for biomass based on root density in 27 soil pits within the Coweeta Hydrologic Laboratory (Table 2 and Figure S1 in the supporting information), which is adjacent to the study site. These pits were selected to sample belowground biomass and/or root distribution of major hardwood species and topographic positions at high elevations, as part of two separate projects [*Hales et al.*, 2009; T. C. Hales and C. F. Miniat, Hillslope-scale root cohesion driven by soil moisture conditions, submitted to *Earth Surface Processes and Landforms*, 2014]. Pits were located on noses (areas of convex downward topography), on side slopes (areas of planar topography), and in hollows (areas of concave upward topography). Identification of the topographic position was primarily made in the field and confirmed by placing accurate global positioning systems measurements of pit locations onto a curvature map derived from the 6.1 m state lidar bare-earth data. Pits in Coweeta subwatershed 28 (WS28) were located in areas that were dominated by several individuals of one of two tree species (*L. tulipifera* or *B. lenta*; Table 2 and Figure S2); both biomass and distribution were measured in these pits. Pits in watershed 36 (WS36) were adjacent to and immediately downslope from several major hardwood species found within the oak-hickory and northern hardwood forest communities; only root distribution was measured in these pits. In WS28, pits were 1×1 m in area, and all roots in ~3 kg of soil encountered were sieved (2 mm mesh), washed, dried, and weighed. To estimate the cross-sectional area of roots intersecting each pit face, we painted roots along a 40 cm wide vertical swath of each pit, photographed, and digitally analyzed to gain the cross-sectional area and coordinates in both studies.

A two-parameter exponential model was fit to the vertical distributions of root area, $A(z)$, from each pit [*Mattia et al.*, 2005; *Preti et al.*, 2010]:

$$A(z) = A_0 e^{-bz}, \tag{1}$$

where A_0 represents root area (m^2) at the surface ($z = 0$), b is the shape parameter (m^{-1}), and z is the soil depth (m). We also estimated root density values across different species, topographic position, and diameters to transform root area to root biomass. We observed dry mass, diameter, and length of the sampled roots. Root density was then estimated from linear regression between root dry mass and volume for all observations ($n = 391$).

2.3. Conversion of Belowground Biomass Map to Total Root Cohesion

Assuming isotropic root distributions, total volume of roots per ground area ($m^3\,m^{-2}$) was calculated by integrating root area over soil depth:

$$V_r = \int_0^\infty A_0 e^{-bz} \cdot dz = \frac{A_0}{b}, \tag{2}$$

The density of roots (ρ_r; $kg\,m^{-3}$) measured for our pit sites (Figure S1) was constant for a range of root densities. We also calculated a constant tensile strength (T_r; $N\,m^{-2}$) across all root diameters based on the linear regression of root tensile force at failure against root cross-sectional area (see *Hales et al.* [2013] for a derivation of the method). Incorporating these parameters, we calculated total belowground biomass per ground area (B_r; $kg\,m^{-2}$) and total root cohesion (C_r) as

$$B_r = \rho_r \frac{A_0}{b}, \tag{3}$$

$$C_r = \int_0^\infty C_r(z) \cdot dz = K \cdot T_r \int_0^\infty A_0 e^{-bz} \cdot dz = K \cdot T_r \frac{A_0}{b}, \tag{4}$$

Table 3. Climate Stations for the Simulation and Available Data Sets

Name	Latitude/Longitude (degree)	Elevation (m)	Source	Available Daily Climate Data
WINE (Wayah Bald)	35.1731/−83.5910	1667	NC Environment and Climate Observing Network (ECONet)	Maximum and minimum temperatures Precipitation Wind speed Solar radiation Relative humidity
NWAY (Wayah)	35.17/−83.40	658	NC Remote Automated Weather Station (RAWS)	Maximum and minimum temperatures Wind speed Solar radiation
Franklin (ID 313228)	35.1803/−83.3925	647	NWS Cooperative Observer (COOP)	Precipitation
Coweeta Hydrologic Lab (CS01)	35.0603/−83.4303	685	USDA Forest Service	Maximum and minimum temperatures Precipitation Wind speed Solar radiation Relative humidity

where $C_r(z)$ is root cohesion (Pa) at soil depth z (m) and K is a constant usually assumed to be 1.2 [*Wu et al*., 1979]. Note that K in this study implicitly includes a dimension converter (m^{-1}) from root volume to area under the assumption of isotropic root distributions. Combining equations (3) and (4),

$$C_r = K \cdot T_r \frac{B_r}{\rho_r}. \tag{5}$$

This method provides a very simple and computationally efficient estimation of the spatial pattern of total belowground biomass and root cohesion.

2.4. Infinite Slope Model

We modeled slope stability using the limit equilibrium infinite slope approach [*Montgomery and Dietrich*, 1994]. The factor of safety (FS) of a slope is defined as a ratio of soil strength (resisting forces) to soil shear stress (driving forces):

$$\mathrm{FS} = \frac{(C_r + C_s) + \cos^2\theta(\rho_s - m\rho_w)D\tan\phi}{\rho_s D \sin\theta\cos\theta}, \tag{6}$$

where C_s is the soil cohesion (kPa), C_r is the cohesive strength supplied by roots (kPa), ϕ is the angle of internal friction of the soil, ρ_s and ρ_w are the unit weights of soil and water ($kg\,m^{-3}$), D is the soil depth (m), and m is the saturated fraction of soil depth. Topographic information required to drive this simple model included slope (θ) and topographic flow paths to derive subsurface flow and resulting saturation levels (for the calculation of m in equation (6)).

2.5. Ecohydrological Model (RHESSys) and Hydrological Records

The Regional Hydro-Ecological Simulation System (RHESSys) is a geographic information system (GIS)-based ecohydrological modeling framework designed to simulate coupled water, carbon, and nitrogen cycling in complex terrain [*Band et al*., 1993; *Tague and Band*, 2004]. RHESSys couples a patch-scale ecosystem model developed from BIOME-BGC [*Running and Hunt*, 1993] and CENTURY [*Parton et al*., 1993] with a distributed hydrologic model that routes water and solutes through topographically defined flow networks connecting patch and hillslope hydrology to the regional stream network. RHESSys was applied to four of five gauged headwater subwatersheds within the study site at a 10 m resolution over a cumulative drainage area of ~145 km^2 (Table 1 and Figure 1) producing ~1.45×10^6 simulation units (patches). These subwatersheds are located at high elevations with steep slopes, mostly covered by deciduous broadleaf and evergreen coniferous forests (Table 1).

Daily climate data from three climate stations (WINE, NWAY, and CS01; Figure 1) were used in the simulations. Details of the climate stations and daily climate data used are summarized in Table 3. For each subwatershed, the model extrapolated daily climate data from the point observation based on topography (elevation,

aspect, and slope) following the MT-CLIM algorithm [*Running et al*., 1987]. Orographic precipitation was estimated from scatterplots of monthly total precipitation between stations assuming a simple linear trend with elevation. Environmental and dewpoint lapse rates were estimated from the scatterplots of daily maximum and minimum temperatures between stations. Stage-discharge rating curves were developed at each gauged subwatershed using a Bayesian multisegment method. Detailed rating curve methods are available in *Price et al*. [2011]. Area-averaged streamflow data for each subwatershed during the period of August 2007 to February 2009 were used for model calibration. Note that flows in the subwatersheds are very flashy, and with limited stage-discharge measurements at high flows, there can be significant uncertainty especially during peak discharge due to the nonlinear nature of rating curves.

2.6. Prescribed Spatiotemporal Dynamics of Vegetation

We estimated spatial patterns of maximum and minimum leaf area index (LAI) for two growing seasons (2 June 2003 and 3 September 2008) and one dormant season (7 March 2004) using Landsat Thematic Mapper (TM) images, all of which are standard level-1 terrain-corrected (L1T) products. The maximum LAI map was derived from the NDVI values by combining two summer images to obtain a composite cloud-free scene (Figure S3). A modified dark object subtraction method was applied to correct atmospheric effects on surface reflectance [*Song et al*., 2001]. The NDVI-LAI relationship was derived from optical (LAI-2000 and hemispheric photos) and historical field measurements (litter traps) of vegetation density in the Coweeta basin [*Hwang et al*., 2009]. Vegetation phenology was prescribed in the model as a function of topographic factors, including elevation, aspect, and topographic wetness index, following *Hwang et al*. [2011]. Landscape phenology models for leaf green-up and senescence were developed at 250 m scale within the study site from 10 year Moderate Resolution Imaging Spectroradiometer NDVI data (2001–2010). The seasonal vegetation dynamics were determined by maximum and minimum LAI values (30 m resolution) and green-up and senescence timing (250 m resolution) without interannual variation.

2.7. Canopy Height Information From Lidar

We use two sources of airborne lidar data in this study, North Carolina statewide lidar (http://www.ncfloodmaps.com) and NCALM (National Center for Airborne Laser Mapping; http://www.ncalm.cive.uh.edu/) lidar data. The North Carolina lidar was used for estimation of canopy structure (tree height) and topographic (bare-earth) information. The state lidar data were collected in 2005 before green-up, to measure bare-earth elevation accurately, provided as a 6.1 m (20 feet) grid format with validations. As the data were collected during a leaf-off period, we used a leaf-on high-resolution NCALM lidar to validate and correct the estimated canopy height map. NCALM lidar data were only available at the Coweeta basin (http://www.opentopography.org), acquired in July 2009, and were used to produce a 1 m resolution canopy height. The NC state lidar bare-earth data at 10 m horizontal resolution are used to delineate the watershed boundaries.

The original data of both state and NCALM lidar included *xyz* coordinates for multiple returns from different parts of the canopy and ground surface. We used *LAStools* (http://www.cs.unc.edu/~isenburg/lastools/) to postprocess the original lidar data. We produced the canopy top elevation map from the first return (or maximum) elevation value within a single 6.1 m pixel, excluding data points classified as building and noise returns. Canopy height was then calculated from the difference between canopy top and bare-earth elevations. The effective count map was also produced as a quality check of this map. However, this method essentially overestimates canopy height because it selects the maximum values within a 6.1 m pixel. The leaf-on canopy heights, derived from NCALM lidar data with the same method, were further compared with those from state lidar data for bias correction. We also related the canopy height information averaged at different window sizes (1×1 to 7×7 m) with observed (or estimated) total belowground biomass values from soil pits ($n = 27$). A summer IKONOS NDVI map (1 June 2003) was also used to correlate with belowground biomass values for the comparison. As developed above, in addition to the belowground biomass, estimates of characteristic root tensile strength (T_r) and density (ρ_r) were then used to generate total root cohesion (C_r) with equation (5).

2.8. Soil Type and Land Cover

Soil depth estimates, required for calculation of the slope stability factor of safety (equation (6)), were extrapolated from depth to refusal measurements at 108 points within the Coweeta Hydrologic Laboratory (Figure S1). Soil depth patterns were estimated with a tree regression model (Figure S4), developed by *Band et al*. [2012]. The estimated soil map may underestimate depths in deeper soils based on the probe length. However,

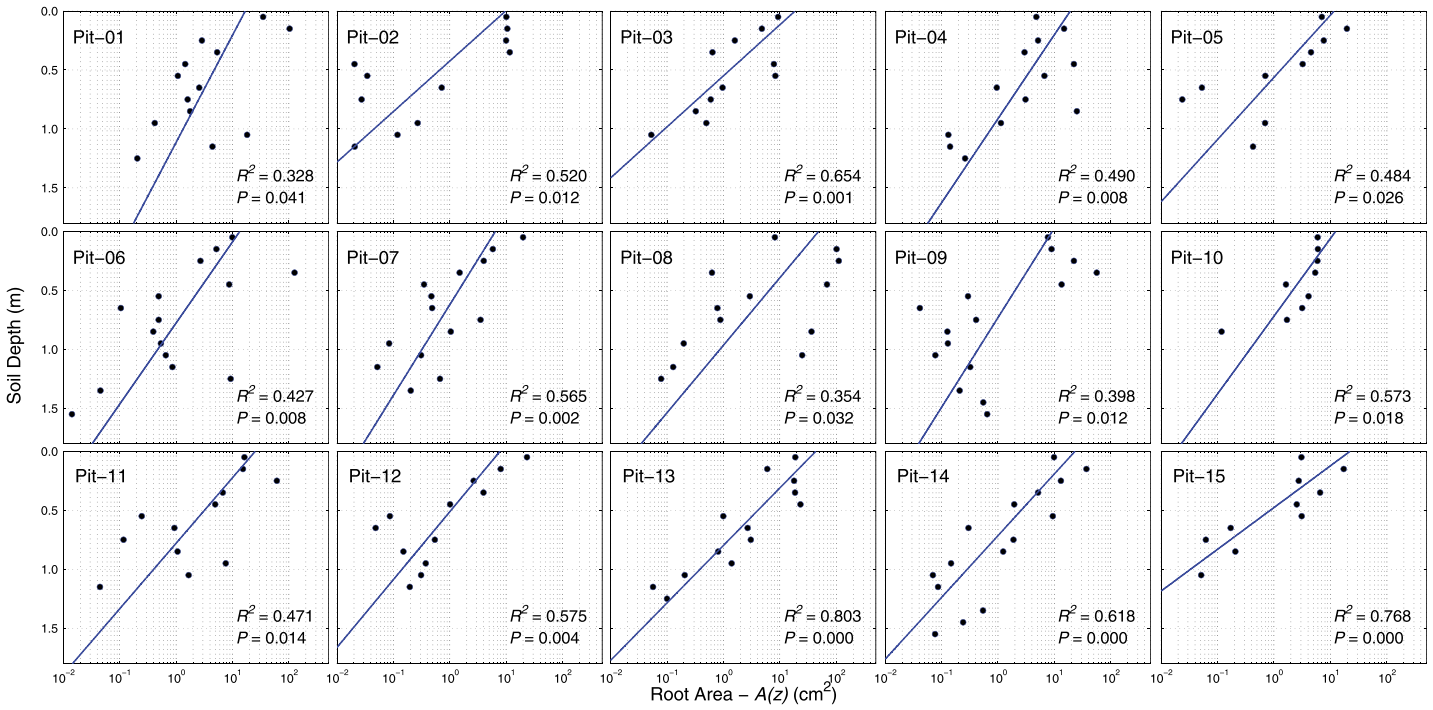

Figure 2. The exponential models of root area (A; cm^2) as a function of soil depth (z; meter) at 15 soil pits at WS36 (Table 2 and Figure S1). Each point represents the total root area at 10 cm intervals. All fitted curves are statistically significant ($p < 0.05$).

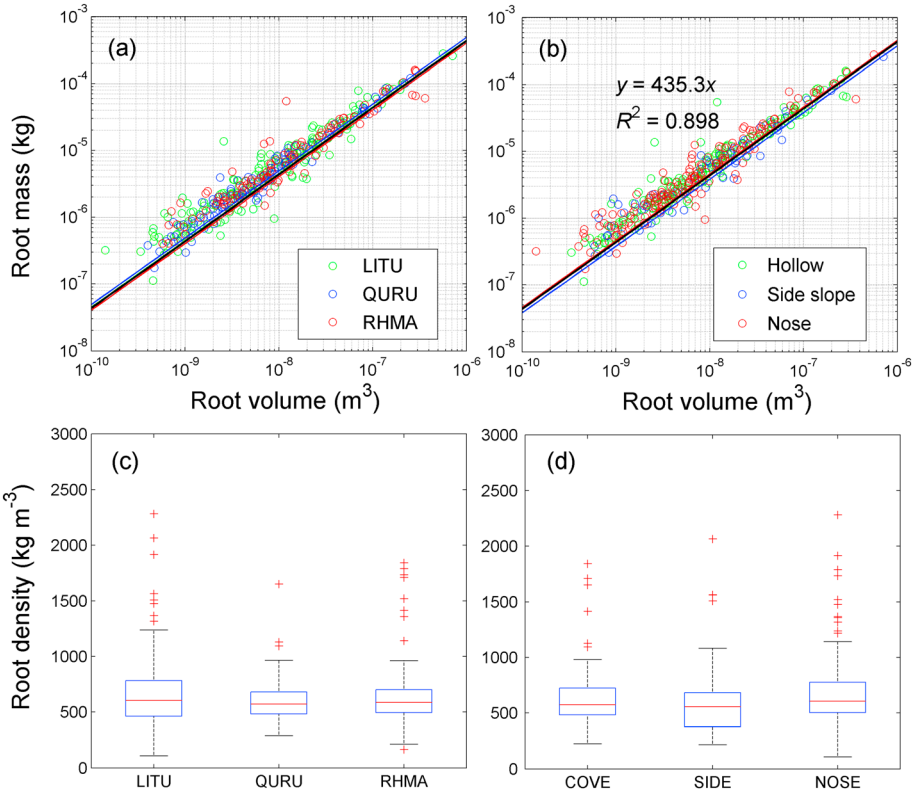

Figure 3. (a) The scatterplots between root volume and dry biomass ($n = 391$) and (b) root density (slope of regression) of different species (LITU, *L. tulipifera*; QURU, *Q. rubra*; and RHMA, *R. maximum*) and at different topographic positions (COVE, hollow; SIDE, side slope; and NOSE, nose).

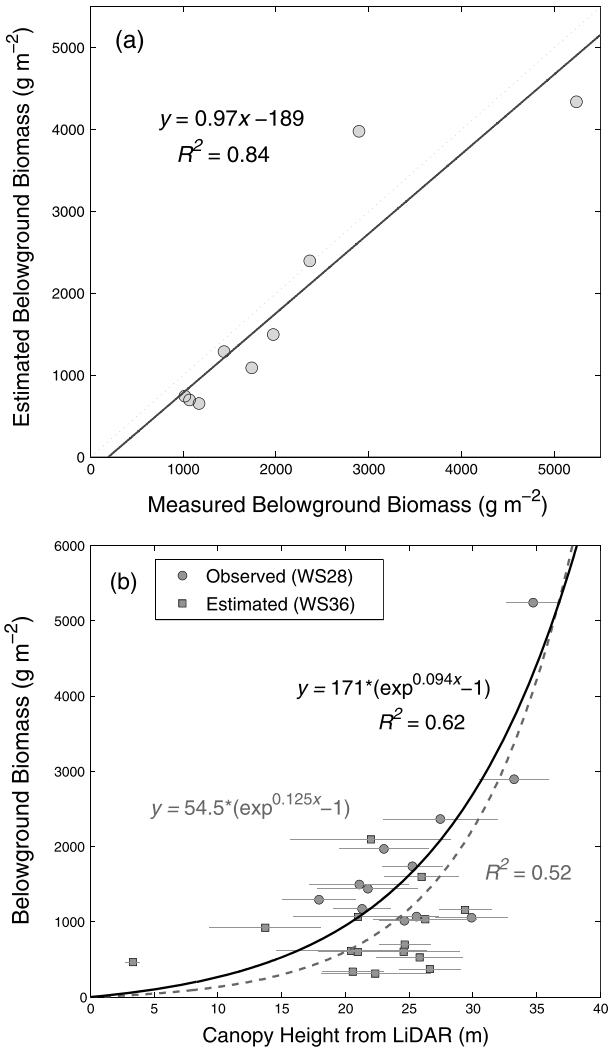

Figure 4. (a) Evaluation of belowground biomass per unit ground area (g m^{-2}) between measured values and estimated from vertical root area distributions at nine soil pits in WS28 and (b) exponential allometric relationships between 3 × 3 m averaged canopy heights from NCALM lidar and belowground biomass values, with (only WS28; $n = 12$; black solid line) and without (WS28 and WS36; $n = 27$; gray dotted line) estimated values. Horizontal bars represent the standard deviations of 1 m canopy height values within 3 × 3 m windows.

reconnaissance in the study area suggests that landslide trigger zones are typically in shallower soils at the very head of hollows. A mean root depth of 0.75 m for tree-based biome types was based on the pit excavations [*Hales et al*., 2009], as insufficient data exist to generate a spatially variable model. The model also incorporated additional GIS information, such as vegetation type, impervious percent, and land use from NLCD (National Land Cover Database), as well as soil type from Soil Survey Geographic Database (Figure S5). The original data sets were rasterized to yield vegetation and soil texture classes required by RHESSys model.

2.9. Model Parameterization and Calibration

The hydrological model was calibrated with six key hydrological parameters: the decay rate of saturated hydraulic conductivity with depth in the soil (for both vertical and lateral dimensions), the saturated hydraulic conductivity at the soil surface (both vertical and lateral), and two conceptual groundwater storage parameters. The model was calibrated for the July 2007 to February 2009 time period with 1.5 years buffering the beginning of simulation, which allows soil water state variables to equilibrate in the model. The Nash-Sutcliffe efficiency of daily log streamflow data [*Nash and Sutcliffe*, 1970] was used as an objective function to identify optimal parameter sets for each watershed as observed peak flows may be unreliable due to rating curve uncertainty. Following calibration, the model was run for a 2 year spin-up, and then for the 2004 period of Hurricanes Frances (7 September) and Ivan (16 and 17 September) and a set of unnamed storms.

RHESSysCalibrator (https://github.com/selimnairb/RHESSysCalibrator) was used to automate the Monte Carlo simulation process. *RHESSysCalibrator* manages (1) generating model parameter sets for each simulation, (2) running simulations using local or high-throughput computing resources, and (3) postprocessing model results to calculate model fitness parameters. Other species-specific ecophysiological parameters were estimated from historical measurements within the Coweeta Hydrologic Laboratory. Details of parameterization are available in *Hwang et al*. [2009, 2012].

2.10. Model Simulation and Evaluation Under Different Root Cohesion Dynamics

A factorial design of FS model simulations were carried out to explore impacts of spatial and temporal dynamics of root cohesion, C_r: (1) spatially and temporally constant C_r, (2) spatially variable and temporally dynamic C_r, and (3) spatially variable and temporally constant C_r. Spatially constant C_r values are obtained by averaging root

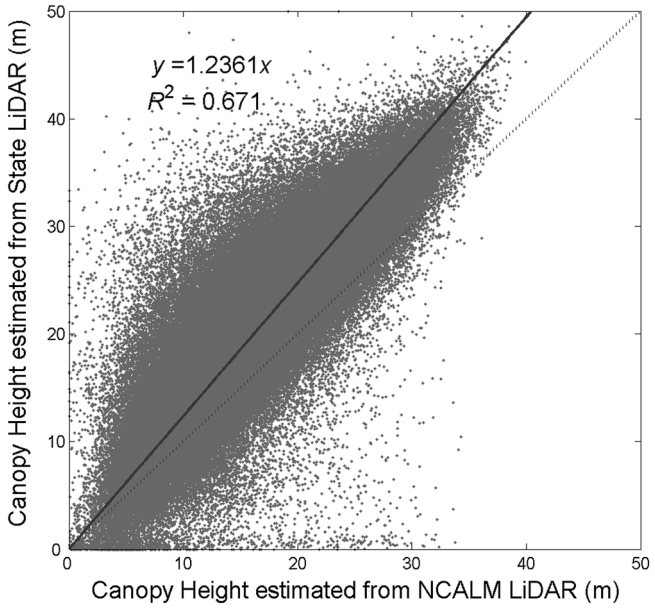

Figure 5. Correlation of canopy heights between averaged 1 m NCALM lidar and estimated from the state lidar at 6.1 m (20 feet) scale.

cohesion values based on Wu method (21.6 kPa) developed by *Hales et al.* [2009]. We also included newly developed estimates of root cohesion incorporating transient adjustment to ambient soil water conditions for temporally dynamic C_r [*Hales et al.*, 2013], providing temporal as well as spatial variability to root strength. Temporally constant C_r for (1) and (3) were calculated assuming near-saturated conditions in time as short-term saturation conditions. Note that the pore pressure levels simulated with the hydrological model were not changed across different root cohesion models.

Rather than attempting to simulate the location of individual slope failures, this study predicts landslides within small subcatchments that would contribute to downstream runout zones, where most damage and hazard are experienced. The presence or absence of failures in a catchment of specified sizes is the prediction target, aggregating over multiple hillslope and hollow features composing the drainage area. To do this, another set of smaller subcatchments was identified with a minimum drainage area of 3 ha (Figure 1; $n = 1388$), which were large enough to identify common potential landslide runout zones over a set of potential initiation sites. Within each subcatchment, the minimum and mean factor of safety (FS) below the 0.5 percentile was obtained at the end of two hurricane events in 2004. Each of these two metrics, the subcatchment event hazard (SEH; SEH_{min} and SEH_{low}, respectively), effectively represents the lower tail of the FS distributions and potential initiation points of shallow landslides within each subcatchment. These subcatchments were subsequently sorted by these metrics and plotted as

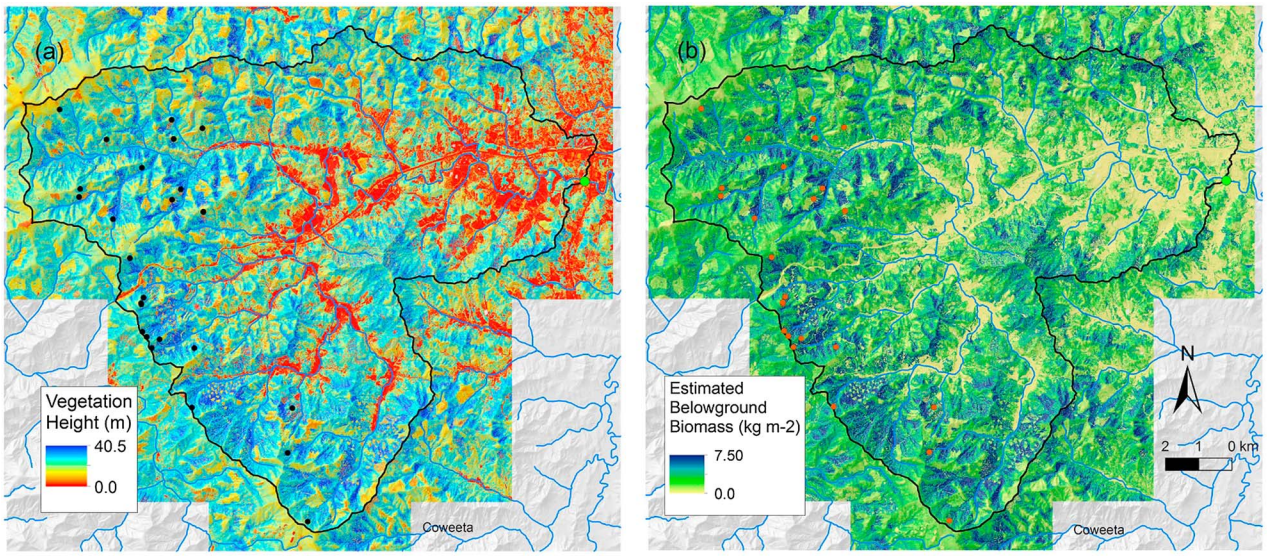

Figure 6. (a) Canopy height (m) from the state lidar and (b) total belowground biomass (kg m^{-2}) using the nonlinear allometric relationship in the study site. The points indicate observed landslide locations from aerial photos and field survey during the two hurricane events in 2004. Note that the maps were not colored at equal intervals of the legends for visual purpose.

Table 4. Nash-Sutcliffe (N-S) Efficiency of Simulated Log and Normal Daily Streamflow for Optimal Simulations at Four Gauged Subwatersheds

Watershed	Wayah Creek	Poplar Cove Creek	Allison Creek	Jones Creek
N-S efficiency for log daily streamflow	0.643	0.305	0.638	0.628
N-S efficiency for daily streamflow	0.569	0.332	0.560	0.678

cumulative distribution functions (CDFs). Each catchment with an observed (mapped) landslide was tagged in the CDF to determine occurrence with the SEH metrics below 1 (predicted failure). This subcatchment-based validation provides an efficient analytical and graphical assessment for landslide predictions generated with different spatial and temporal variability of root cohesion.

3. Results

3.1. Root Vertical Distributions

Vertical root area distributions at 10 cm intervals in 15 soil pits within WS36 declined exponentially with soil depth (Figure 2; $P < 0.05$). For the pits in WS28 that were arrayed by species and topography, we found that two parameters of the exponential model (A_0 and b; equation (1)) did not differ significantly by topographic positions (hollow or nose) or species (*L. tulipifera* or *B. lenta*; not shown here). The A_0 parameter represents the absolute total area of roots, while the b parameter is related to the shape of the fitted curve, with higher values representing faster decline of root area with depth.

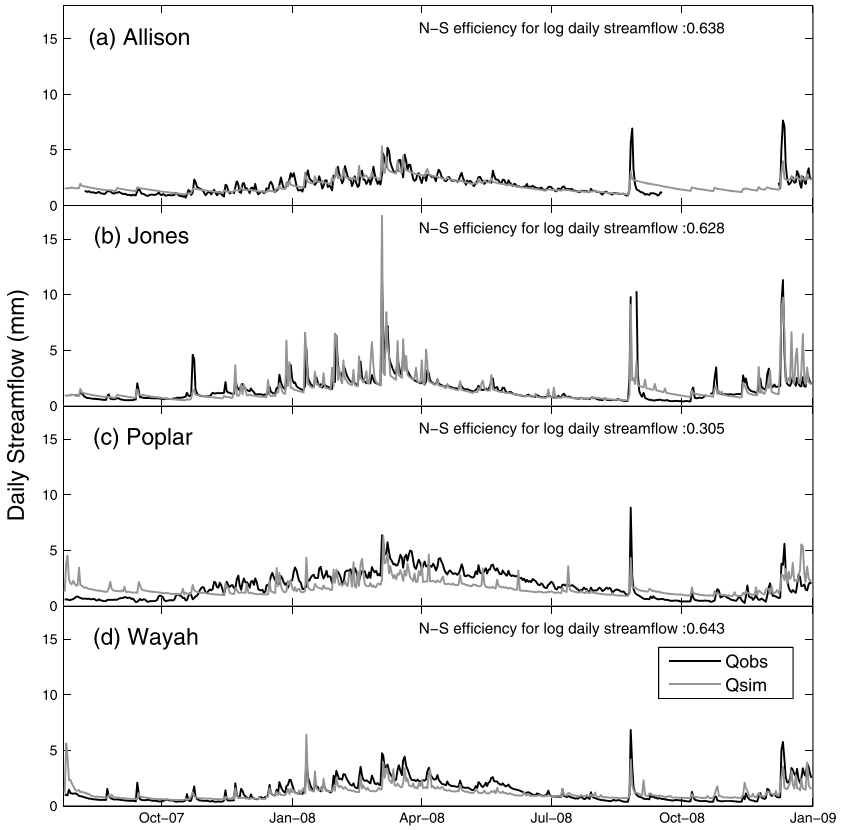

Figure 7. Observed (Q_{obs}) and simulated (Q_{sim}) daily streamflow at the four subwatersheds (Table 1 and Figure 1) in the study site during the calibration period (July 2007 to December 2008). N-S represents the Nash-Sutcliffe efficiency between log-transformed observed and simulated daily streamflow.

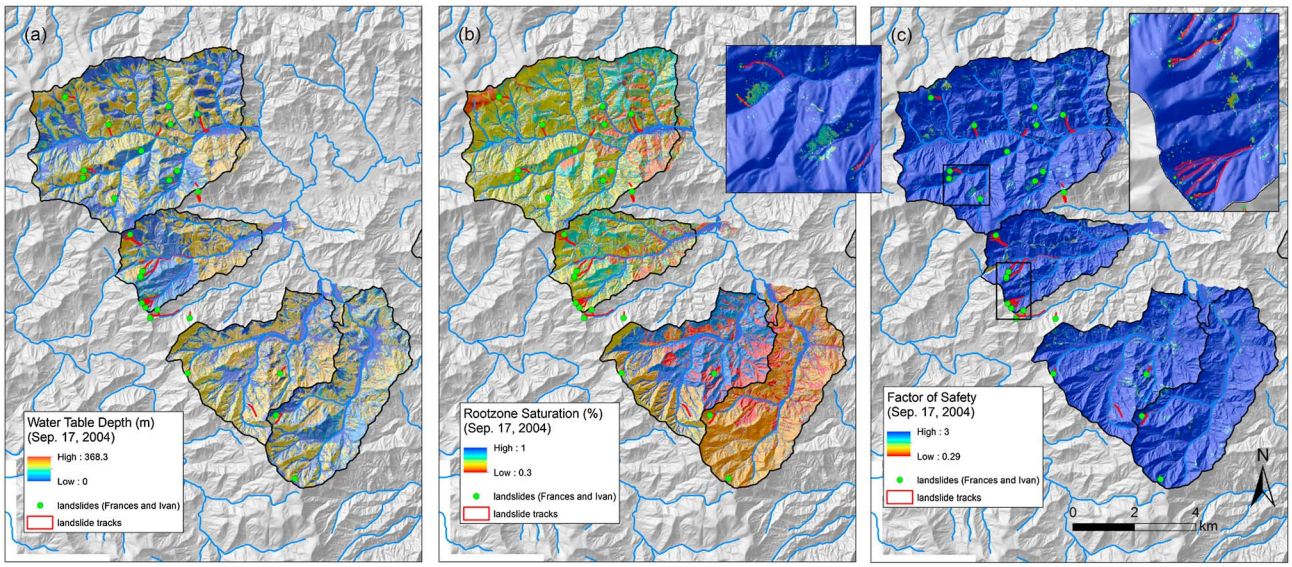

Figure 8. (a) Simulated water table depth (m), (b) root zone saturation percent (%), and (c) calculated factor of safety (FS) on 17 September 2004 immediately after the second hurricane event (Ivan). Windowed regions for FS are located in two squares. Points and polygons indicate observed landslide locations and tracks from aerial photos and field survey during the two hurricane events (Frances and Ivan) in 2004. Note that the maps are not colored with equal intervals within legends for visual purpose.

3.2. Total Belowground Biomass and Root Properties From Soil Pits

Observed total belowground biomass values by topography and species are shown in Table 2. The number of observations ($n = 12$) was not large enough to discern statistical differences among different groups (topography and species). Root volume and mass were linearly related ($R^2 = 0.90$), where the slope (435.3 kg m^{-3}) effectively represents the average density of roots in the study site (Figure 3). Root density among the three different species (*L. tulipifera*, *Q. rubra*, and *R. maximum*) at different topographic positions (nose, side slope, and hollows) did not differ, supporting the use of a constant root density for conversion of root volume to biomass in equation (3). We also found good agreement between total belowground biomass values estimated from equation (3) and vertical root distribution at the nine WS28 pits (Figure 4a; $R^2 = 0.84$).

3.3. Canopy Height and Belowground Biomass Maps From Lidar

Taller trees had exponentially more belowground biomass than shorter trees (Figure 4b). The nonlinear relationship was strongest when a 3×3 m lidar resolution was used to estimate canopy height ($R^2 = 0.62$; $n = 12$). This suggests that canopy height is a good indicator for canopy growth stage and subsequent aboveground and belowground biomass [*Lefsky et al.*, 2002, 2005]. While the 6.1 m scale canopy heights from the state lidar were strongly correlated with average values of the 1 m heights from NCALM lidar within each 6.1 m pixel ($R^2 = 0.67$), they overestimated height by ~24% (Figure 5). We used a bias correction of the canopy height estimates from the state lidar to produce a canopy height map at the 6.1 m scale (Figure 6a). The final canopy heights were well within the ranges of field-observed canopy height values in the study site (less than about 40 m) [*Dietze et al.*, 2008; *Henning and Radtke*, 2006]. Canopy height was usually higher in midslopes compared to ridge tops and valley bottoms. We then produced a total belowground biomass map (Figure 6b) and a root cohesion map using equation (5). The effective counts of point lidar measurements within a single 6.1 m spatial scale showed strong patterns with elevation (not shown here), suggesting that the sensor retrieved more effective returns at high elevations. Note that the larger effective counts in higher elevation regions improved the accuracy of the derived canopy information for the regions susceptible to landslides.

3.4. Hydrological Model Performance

We found fairly good agreement between observed and simulated daily streamflow on seasonal and event scales (Table 4 and Figure 7) although there were large uncertainties in the rating curves and spatial precipitation inputs within the mountainous study watersheds. The model produced the poorest result at Poplar Cove Creek where there was no nearby climate station (Figure 1). Simulated water table depths and

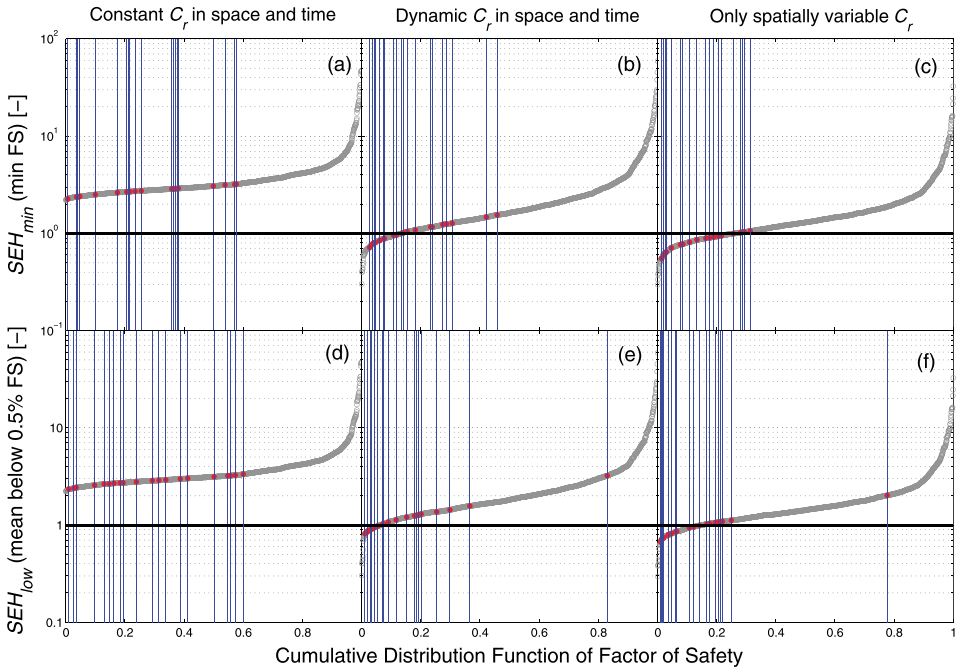

Figure 9. Cumulative distribution functions of the minimum (SEH_{min}) and the mean below 0.5 percentile (SEH_{low}) of the factor of safety (FS) at the subcatchment scale ($n = 1388$). (a and d) Constant root cohesion (C_r) in space and time, (b and e) dynamic root C_r in space and time, and (c and f) spatially variable and temporally constant C_r under the near-saturation assumption. Vertical lines and red dots at the cross sections represent the subcatchments ($n = 24$), where landslide events were observed during the two hurricane events (Frances and Ivan) in 2004.

root zone saturation at the end of this period on 17 September (Figures 8a and 8b) were substituted into equation (6) along with all other soil and root strength information to solve for factor of safety (FS) at 10 m spatial resolution (Figure 8c).

3.5. Prediction for Slope Failures Within Subcatchments

The model predicted low FS (and high hazard, FS < 1) around the actual initiation points and their tracks following the second hurricane event (17 September 2004; see Figure 8c insets). Cumulative distribution functions (CDFs) of the two subcatchment event hazard metrics, SEH_{min} and SEH_{low}, over all subcatchments ($n = 1388$) are presented in Figure 9 along with observed failures. Localization of predicted event landslide hazard to small subcatchment areas minimizes the number of recorded subcatchment events with SEH > 1 (errors of omission), maximizing the number of events with SEH < 1. An even distribution of events above and below SEH $= 1$ would indicate no skill in prediction. Under the assumption of constant C_r of 22 kPa, no subcatchment was predicted to produce min values of SEH < 1 at the end of two hurricane events (Figure 9a), indicating that a constant C_r poorly predicted the relative distribution of actual landslide events. Sensitivity analysis to different constant C_r values showed similar results, only shifting the CDF line vertically (trading errors of omission for errors of commission). With a constant C_r, landslides still occurred at the 60th percentile of SEH_{min} at the subcatchment scale, meaning that 60% of the subcatchments would be predicted and mapped with high event hazard to include all observed landslides.

The spatiotemporal dynamics of root cohesion strongly affects the predicted hazard, both in terms of the number and the percentage of high event hazard subcatchments ($SEH_{min} < 1$; Figure 9b). However, the best prediction results occurred when only the spatial variation of root cohesion was incorporated in FS calculations with a minimum root tensile strength (near-saturated conditions; Figure 9c). The model predicted most of the landslides that occurred in 2004 with less than 25% of the subcatchments rated at $SEH_{min} < 1$ to include all observed landslides. This model provided the best result, not only improving the absolute proportion of the subcatchments that was predicted to be failure prone but also reducing

significantly the proportion of the subcatchments that would have a minimum FS < 1 to include all of the 2004 landslides. Similar results were also produced using the SEH_{low} metric (Figures 9d–9f).

4. Discussion

4.1. Belowground Root Information for Spatial Landslide Modeling

Although there have been several studies to model spatial patterns of root cohesion at tree [*Roering et al*., 2003; *Sakals and Sidle*, 2004] and landscape scales [*Ji et al*., 2012; *Mao et al*., 2012], there are few that characterize regional-scale root cohesion patterns using remote sensing data. Typically, uniform or random distributions of root cohesion are applied to soil erosion or landslide models. The magnitude of these parameters can then be calibrated using existing landslide data sets. For our initial runs, we applied an average root cohesion based on the application of Wu method for 15 soil pits in North Carolina [*Hales et al*., 2009]. Using this value, no landslides were predicted: evidently, the cohesion value was too high. Numerous studies suggest that the Wu method overestimates the magnitude of root reinforcement and that the fiber bundle method produces more physically meaningful representations of root cohesion [*Pollen-Bankhead and Simon*, 2009; *Schwarz et al*., 2010]. However, if we reduced the magnitude of root cohesion and apply it uniformly across the landscape, there would be considerable overestimation of the potential areas of failure. In our simulation results, to fit most or all of the extant landslides, it would require a cohesion value that would result in 50–60% of the subcatchments having minimum FS < 1 (Figures 9a and 9d), a considerable over exaggeration which could lead to significant error in hazard prediction.

For the spatially variable and temporally constant C_r model (Figures 9c and 9f), we applied the Wu method of root cohesion based on spatially distributed root biomass and assigned the weakest root tensile strengths, essentially assuming that the shallow soil column was saturated everywhere. Allowing root cohesion to vary in time as a function of simulated soil moisture did not improve the model accuracy (Figures 9b and 9e). This suggests that the distribution of root biomass exerts a greater control on root cohesion than root tensile strength. While the direct simulations of pore pressures with spatially variable C_r showed greater predictive skill than with spatially constant C_r, there were more errors of omission of unstable conditions compared to model runs with the saturation assumption. This also suggests that the distributed ecohydrological model effectively simulated the spatial patterns of shallow subsurface flows during the event, but that the model may not have captured short-term near-saturation conditions in shallow soils due to coarse precipitation inputs (daily) and vertical soil representation.

4.2. Remote Sensing of Aboveground Vegetation

Remote sensing of spectral information has significantly improved the estimation of aboveground vegetation information, including leaf area index, canopy cover, and aboveground biomass [e.g., *Lu*, 2005; *Tucker*, 1979]. However, these optical canopy properties are less reliable for the estimation of aboveground biomass [e.g., *Sellers*, 1985]. *Kobayashi et al*. [2012] reported that NDVI even decreased with forest growth (after 2–3 years), possibly related to backscattering and shading effect with increasing tree heights. Traditionally, forest inventory data, such as diameter at breast height (DBH), tree height, crown size, or tree ages, are more accurate predictors for aboveground biomass information using allometric equations, especially in mature forested ecosystems [e.g., *Martin et al*., 1998]. For this reason, many researchers have used supplementary forest inventory data to estimate aboveground biomass with spectral remote sensing data [*Hall et al*., 2006; *Muukkonen and Heiskanen*, 2005, 2007; *Powell et al*., 2010; *Zheng et al*., 2004].

Lidar systems provide more direct measurements of canopy structure, compared to traditional passive remote sensing imagery. Vegetation height is typically positively correlated with tree age and thus closely associated with forest growth stage. Therefore, older trees have more belowground biomass (and resulting root cohesion) than younger trees. This study effectively showed that landslide probability should decrease with tree age. Several studies in the Pacific Northwest also report higher landslide density in younger, compared to older, forests [*Turner et al*., 2010]. Recently, *Milodowski et al*. [2015] found that erosion rates in Sierra Nevada Mountains increased with lower aboveground biomass values, estimated from lidar-derived vegetation height. In this sense, extension of aboveground canopy information to subsurface biomass and erosion rates holds the potential for another major advance in distributed modeling for landslide hazards.

4.3. Allocation Dynamics in Space and Time

Allocation ratio sets the amount of predicted belowground biomass and resulting root properties for a given aboveground biomass. However, the proportional belowground allocation typically increases with fewer belowground resources available [*Cromer and Jarvis*, 1990; *Gedroc et al*., 1996; *McConnaughay and Coleman*, 1999]. Therefore, allocation ratios may vary in space and time with topographic positions, species, ages, and vegetation growth. Note that the data in our study site included different topographic positions and species (Table 2), which may explain some of the scatter from the regression line between canopy height and belowground biomass (Figure 4b). In addition, the relation between tree height and belowground biomass was generated at a landscape level (not at the individual tree level) and did not consider differences in stem density (Figure S2).

The exponential relationship between canopy height and belowground biomass corresponds to the allometric relationships between diameters at breast height (DBH), canopy height, and aboveground biomass in the study site [*Henning and Radtke*, 2006; *Martin et al*., 1998; *Vieilledent et al*., 2010]. This potential nonlinearity between aboveground and belowground biomass might also be related to the decline in aboveground allocation with stand age after canopy closure. This phenomenon is usually called "ontogenic drift" [*McConnaughay and Coleman*, 1999], which indicates that the fraction of gross primary production partitioned to belowground biomass increases with stand age [e.g., *Ryan et al*., 2004]. How we incorporate these dynamic allocation schemes, based on optimality and ontogeny, may be a big challenge in accurate estimation of root properties from remotely sensed aboveground vegetation information.

4.4. Increased Landslide Vulnerability in the Southern Appalachians

Potential of increased vulnerability to landslides can be outlined for the southern Appalachians (and other regions) over the near to long term: mountain roads, nonrandom species loss or expansion, and climate change. First, over the past two decades, there has been a large expansion of the high-elevation road network, commonly as private drives, as a function of second home development. Altered drainage and steepening of slopes tend to concentrate surface and shallow subsurface flow, as roadcuts intercept upslope flow and drain flow through culverts. These locally affect both pore pressures and slope forces in equation (6), and many landslides are associated with road development. Second, rhododendron is an evergreen shrub with shallow roots that has responded to disturbances by expanding its spatial distribution [*Elliott and Vose*, 2012] and growth rate [*Ford et al*., 2012]. Rhododendron transpires less water than other hardwood tree species, potentially providing wetter antecedent conditions and less root cohesive strength [*Brantley et al*., 2014; *Nilsen*, 1985]. Lastly, there is good evidence that there is an increase in the frequency of intense precipitation events in the recent past, which is consistent with the expectations of a warming climate and increased hydroclimate variability [*Huntington*, 2006; *Seager et al*., 2009]. The combination of these trends requires methods to incorporate fine-scale hydrologic flow routing for road systems and the ability to measure canopy composition and structure and directly incorporate these measurements as physiologic differences in plant water use and rooting depths and sufficiently resolve space and time precipitation variability into localized saturation events. While the current results point to specific improvements in landslide hazard forecasting, ongoing research is targeting all three of these areas of increased vulnerability.

4.5. Future Landslide Hazard Forecasting

The methods we have incorporated into the ecohydrologic and landslide modeling are simplified for large-scale application, which assume shallow slope parallel flow and use of a single, composite cohesive strength derived from root tensile strength. Recent research has also emphasized more detailed, three-dimensional modeling of hydrologic contributions and root cohesion to pore pressure development. *Montgomery et al*. [2009], using detailed measurements of flow patterns within hillslopes resulting in an observed slope failure, found that explanation and derivation of the pore pressure prior to failure required both a much greater amount of information on subsurface structure and more detailed modeling than the simple two-dimension plane parallel assumptions commonly used. *Mao et al*. [2014] also compared the effect of root traits, such as orientation, position, type, and normal pressure, using two numerical modeling approaches and suggested that the existing root reinforcement models tended to overestimate root cohesion. Although detailed lidar data can generate stem-level vegetation information, such as crown size and stem density, our data available for the Cartoogechaye watershed did not have the resolution fine enough for those analyses. More

sophisticated three-dimensional root structural modeling linked to detailed aboveground vegetation information would help to improve this relationship for future studies.

Another key variable to improve landslide prediction is precipitation. Improvements in quantitative precipitation estimation (QPE) and short-term quantitative precipitation forecasting (QPF), in addition to informatics necessary to bring together the spatial data required for these modeling approaches are being further explored for increased landslide prediction skill. Improvements in QPE and QPF in mountainous areas are a current emphasis of meteorological instrumentation and modeling in the southern Appalachians and have the potential to significantly improve the spatial and temporal resolution of landslide forecasting (http://hmt.noaa.gov/field_programs/hmt-se/). We used a period of repeated, large subtropical storms in the southern Appalachians, with low return period. September of 2004 had repeated hurricanes and other storms in quick succession in late summer, including Hurricanes Frances and Ivan, which caused numerous landslides. For these conditions, saturation events may be experienced due to high antecedent moisture conditions and very localized, high-precipitation cells embedded in the overall storm and boosted by orographic effects. Measurement of spatial variation in precipitation is sparse in this area, such that the highest rates are likely underestimated.

5. Conclusions

In this study, we used forest ecophysiological measurements, modeling, and field investigations to develop estimates of belowground biomass patterns to generate root strength parameters. We developed a simple analytical solution to predict the spatial distribution of root cohesive strength from lidar-derived canopy information with a sample of measured root distributions and compared the ability to localize landslide occurrence for a specific set of storm events to small subcatchments with methods that assume spatially uniform or variable root strength. This study suggests that canopy height information from lidar can be effectively used to derive spatial patterns of belowground biomass and root cohesion, with consequent improvement of predictive skill for forecasting of shallow landslides in forested catchments. The factor of safety (FS) simulations between spatially constant and variable root cohesion showed that topography alone (e.g., upslope contributing area and surface slope) was not sufficient to model landslide occurrence accurately in this area and that by allowing root cohesion to vary spatially, landslide prediction improved significantly.

For the objectives posed in the study: we report that (1) recent development of lidar remote sensing is effective in estimating spatial root cohesion patterns and (2) incorporation of the spatial covariance between topography, soils, and vegetation belowground information improves skill for slope stability mapping and prediction. This study was designed to develop methods of estimating vegetation aboveground and belowground canopy contributions to root cohesive strength and transient hydrologic conditions, integrated into a distributed simulation framework coupling the ecosystem patterns and processes with the production of runoff, soil moisture, shallow groundwater, and pore pressure patterns. As a coupled modeling approach, the methods presented have the capacity to estimate multiple ecosystem services under a unified modeling framework, including freshwater availability, forest carbon sequestration, and the regulation of landslides, flooding, and erosion. In terms of prediction scales, our approach strikes a compromise between large-area, long-term assessment of landslide hazard zones and site-specific prediction of landslide potential to specific events.

Acknowledgments

We thank two anonymous reviewers who provided helpful comments on the manuscript. We also thank Dean Urban of Duke University for use of his soil depth data set and Rick Wooten of the North Carolina Geological Survey for sharing data on mapped failure locations. All data and simulation results in this paper are available from the authors upon requests. Spatial (GIS and lidar) data and model source codes (RHESSys and *RHESSysCalibrator*) are available from URL links cited in the paper. This study was funded by the USDA Forest Service, Southern Research Station, and National Science Foundation grant DEB-0823293 from the Long Term Ecological Research Program to the Coweeta LTER Program at the University of Georgia.

References

Band, L. E., P. Patterson, R. Nemani, and S. W. Running (1993), Forest ecosystem processes at the watershed scale: Incorporating hillslope hydrology, *Agric. For. Meteorol.*, *63*(1–2), 93–126.

Band, L. E., T. Hwang, T. C. Hales, J. Vose, and C. Ford (2012), Ecosystem processes at the watershed scale: Mapping and modeling ecohydrological controls of landslides, *Geomorphology*, *137*(1), 159–167.

Benda, L., and T. Dunne (1997), Stochastic forcing of sediment supply to channel networks from landsliding and debris flow, *Water Resour. Res.*, *33*(12), 2849–2863, doi:10.1029/97WR02388.

Berti, M., M. L. V. Martina, S. Franceschini, S. Pignone, A. Simoni, and M. Pizziolo (2012), Probabilistic rainfall thresholds for landslide occurrence using a Bayesian approach, *J. Geophys. Res.*, *117*, F04006, doi:10.1029/2012JF002367.

Brantley, S. T., C. F. Miniat, K. J. Elliott, S. H. Laseter, and J. M. Vose (2014), Changes to southern Appalachian water yield and stormflow after loss of a foundation species, *Ecohydrology*, doi:10.1002/eco.1521.

Chen, H., and C. F. Lee (2003), A dynamic model for rainfall-induced landslides on natural slopes, *Geomorphology*, *51*(4), 269–288.

Cromer, R. N., and P. G. Jarvis (1990), Growth and biomass partitioning in eucalyptus-grandis seedlings in response to nitrogen supply, *Aust. J. Plant Physiol.*, *17*(5), 503–515.
Day, F. P., D. L. Philips, and C. D. Monk (1988), Forest communities and patterns, in *Forest Hydrology and Ecology at Coweeta*, edited by W. T. Swank and J. D. A. Crossley, pp. 141–149, Springer, New York.
Dietze, M. C., M. S. Wolosin, and J. S. Clark (2008), Capturing diversity and interspecific variability in allometries: A hierarchical approach, *For. Ecol. Manage.*, *256*(11), 1939–1948.
Elliott, K. J., and J. M. Vose (2012), Age and distribution of an evergreen clonal shrub in the Coweeta basin: Rhododendron maximum L, *J. Torrey Bot. Soc.*, *139*(2), 149–166.
Ford, C. R., and J. M. Vose (2007), *Tsuga canadensis* (L.) Carr. mortality will impact hydrologic processes in southern Appalachian forest ecosystems, *Ecol. Appl.*, *17*(4), 1156–1167.
Ford, C. R., K. J. Elliott, B. D. Clinton, B. D. Kloeppel, and J. M. Vose (2012), Forest dynamics following eastern hemlock mortality in the southern Appalachians, *Oikos*, *121*(4), 523–536.
Fuhrmann, C. M., C. E. Konrad II, and L. E. Band (2008), Climatological perspectives on the rainfall characteristics associated with landslides in western North Carolina, *Phys. Geogr.*, *29*(4), 289–305.
Gedroc, J. J., K. D. M. McConnaughay, and J. S. Coleman (1996), Plasticity in root shoot partitioning: Optimal, ontogenetic, or both?, *Funct. Ecol.*, *10*(1), 44–50.
Ghestem, M., R. C. Sidle, and A. Stokes (2011), The influence of plant root systems on subsurface flow: Implications for slope stability, *BioScience*, *61*(11), 869–879.
Glade, T. (2003), Landslide occurrence as a response to land use change: A review of evidence from New Zealand, *Catena*, *51*(3), 297–314.
Hales, T. C., C. R. Ford, T. Hwang, J. M. Vose, and L. E. Band (2009), Topographic and ecologic controls on root reinforcement, *J. Geophys. Res.*, *114*, F03013, doi:10.1029/2008JF001168.
Hales, T. C., C. Cole-Hawthorne, L. Lovell, and S. L. Evans (2013), Assessing the accuracy of simple field based root strength measurements, *Plant Soil*, *372*(1-2), 553–565.
Hall, R. J., R. S. Skakun, E. J. Arsenault, and B. S. Case (2006), Modeling forest stand structure attributes using Landsat ETM+ data: Application to mapping of aboveground biomass and stand volume, *For. Ecol. Manage.*, *225*(1–3), 378–390.
Henning, J. G., and P. J. Radtke (2006), Ground-based laser imaging for assessing three-dimensional forest canopy structure, *Photogramm. Eng. Remote Sens.*, *72*(12), 1349–1358.
Huntington, T. G. (2006), Evidence for intensification of the global water cycle: Review and synthesis, *J. Hydrol.*, *319*(1–4), 83–95.
Hwang, T., L. E. Band, and T. C. Hales (2009), Ecosystem processes at the watershed scale: Extending optimality theory from plot to catchment, *Water Resour. Res.*, *45*, W11425, doi:10.1029/2009WR007775.
Hwang, T., C. Song, J. M. Vose, and L. E. Band (2011), Topography-mediated controls on local vegetation phenology estimated from MODIS vegetation index, *Landscape Ecol.*, *26*(4), 541–556.
Hwang, T., L. E. Band, J. M. Vose, and C. Tague (2012), Ecosystem processes at the watershed scale: Hydrologic vegetation gradient as an indicator for lateral hydrologic connectivity of headwater catchments, *Water Resour. Res.*, *48*, W06514, doi:10.1029/2011WR011301.
Ji, J., N. Kokutse, M. Genet, T. Fourcaud, and Z. Zhang (2012), Effect of spatial variation of tree root characteristics on slope stability. A case study on Black Locust (*Robinia pseudoacacia*) and Arborvitae (*Platycladus orientalis*) stands on the Loess Plateau, China, *Catena*, *92*, 139–154.
Kobayashi, S., R. Widyorini, S. Kawai, Y. Omura, K. Sanga-Ngoie, and B. Supriadi (2012), Backscattering characteristics of L-band polarimetric and optical satellite imagery over planted acacia forests in Sumatra, Indonesia, *J. Appl. Remote Sens.*, *6*(1), 063525, doi:10.1117/1.JRS.6.063525.s
Laseter, S. H., C. R. Ford, J. M. Vose, and L. W. Swift (2012), Long-term temperature and precipitation trends at the Coweeta Hydrologic Laboratory, Otto, North Carolina, USA, *Hydrol. Res.*, *43*(6), 890.
Lee, A. C., and R. M. Lucas (2007), A lidar-derived canopy density model for tree stem and crown mapping in Australian forests, *Remote Sens. Environ.*, *111*(4), 493–518.
Lefsky, M. A., W. B. Cohen, D. J. Harding, G. G. Parker, S. A. Acker, and S. T. Gower (2002), lidar remote sensing of above-ground biomass in three biomes, *Global Ecol. Biogeogr.*, *11*(5), 393–399.
Lefsky, M. A., D. J. Harding, M. Keller, W. B. Cohen, C. C. Carabajal, F. D. Espirito-Santo, M. O. Hunter, and R. de Oliveira (2005), Estimates of forest canopy height and aboveground biomass using ICESat, *Geophys. Res. Lett.*, *32*, L22S02, doi:10.1029/2005GL023971.
Lehmann, P., and D. Or (2012), Hydromechanical triggering of landslides: From progressive local failures to mass release, *Water Resour. Res.*, *48*, W03535, doi:10.1029/2011WR010947.
Litton, C. M., J. W. Raich, and M. G. Ryan (2007), Carbon allocation in forest ecosystems, *Global Change Biol.*, *13*(10), 2089–2109.
Lu, D. (2005), Aboveground biomass estimation using Landsat TM data in the Brazilian Amazon, *Int. J. Remote Sens.*, *26*(12), 2509–2525.
Mao, Z., C. Jourdan, M.-L. Bonis, F. Pailler, H. Rey, L. Saint-André, and A. Stokes (2012), Modelling root demography in heterogeneous mountain forests and applications for slope stability analysis, *Plant Soil*, *363*(1–2), 357–382.
Mao, Z., M. Yang, F. Bourrier, and T. Fourcaud (2014), Evaluation of root reinforcement models using numerical modelling approaches, *Plant Soil*, *381*(1–2), 249–270.
Martin, J. G., B. D. Kloeppel, T. L. Schaefer, D. L. Kimbler, and S. G. McNulty (1998), Aboveground biomass and nitrogen allocation of ten deciduous southern Appalachian tree species, *Can. J. For. Res.*, *28*(11), 1648–1659.
Mattia, C., G. B. Bischetti, and F. Gentile (2005), Biotechnical characteristics of root systems of typical Mediterranean species, *Plant Soil*, *278*(1–2), 23–32.
McConnaughay, K. D. M., and J. S. Coleman (1999), Biomass allocation in plants: Ontogeny or optimality? A test along three resource gradients, *Ecology*, *80*(8), 2581–2593.
Miller, A. J. (2013), Remote sensing proxies for deforestation and soil degradation in landslide mapping: A review, *Geogr. Compass*, *7*(7), 489–503.
Milodowski, D. T., M. M. Simon, and E. T. A. Mitchard (2015), Erosion rates as a potential bottom-up control of forest structural characteristics in the Sierra Nevada Mountains, *Ecology*, *96*, 31–38, doi:10.1890/14-0649.1.
Montgomery, D. R., and W. E. Dietrich (1994), A physically based model for the topographic control on shallow landsliding, *Water Resour. Res.*, *30*(4), 1153–1171, doi:10.1029/93WR02979.
Montgomery, D. R., K. M. Schmidt, H. M. Greenberg, and W. E. Dietrich (2000), Forest clearing and regional landsliding, *Geology*, *28*(4), 311–314.
Montgomery, D. R., K. M. Schmidt, W. E. Dietrich, and J. McKean (2009), Instrumental record of debris flow initiation during natural rainfall: Implications for modeling slope stability, *J. Geophys. Res.*, *114*, F01031, doi:10.1029/2008JF001078.

Muukkonen, P., and J. Heiskanen (2005), Estimating biomass for boreal forests using ASTER satellite data combined with standwise forest inventory data, *Remote Sens. Environ.*, *99*(4), 434–447.
Muukkonen, P., and J. Heiskanen (2007), Biomass estimation over a large area based on standwise forest inventory data and ASTER and MODIS satellite data: A possibility to verify carbon inventories, *Remote Sens. Environ.*, *107*(4), 617–624.
Nash, J. E., and J. V. Sutcliffe (1970), River flow forecasting through conceptual models part I — A discussion of principles, *J. Hydrol.*, *10*(3), 282–290.
Nilsen, E. T. (1985), Seasonal and diurnal leaf movements of *Rhododendron maximum* L. in contrasting irradiance environments, *Oecologia*, *65*(2), 296–302.
Pack, R. T., D. G. Tarboton, C. N. Goodwin, and A. Prasad (2005), SINMAP 2. A stability index approach to terrain stability hazard mapping, technical description and users guide for version 2.0, Utah State Univ.
Parton, W. J., et al. (1993), Observations and modeling of biomass and soil organic-matter dynamics for the grassland biome worldwide, *Global Biogeochem. Cycles*, *7*(4), 785–809, doi:10.1029/93GB02042.
Pollen-Bankhead, N., and A. Simon (2009), Enhanced application of root-reinforcement algorithms for bank-stability modeling, *Earth Surf. Processes Landforms*, *34*(4), 471–480.
Popescu, S. C., and R. H. Wynne (2004), Seeing the trees in the forest, *Photogramm. Eng. Remote Sens.*, *70*(5), 589–604.
Popescu, S. C., R. H. Wynne, and R. F. Nelson (2003), Measuring individual tree crown diameter with lidar and assessing its influence on estimating forest volume and biomass, *Can. J. Remote Sens.*, *29*(5), 564–577.
Powell, S. L., W. B. Cohen, S. P. Healey, R. E. Kennedy, G. G. Moisen, K. B. Pierce, and J. L. Ohmann (2010), Quantification of live aboveground forest biomass dynamics with Landsat time-series and field inventory data: A comparison of empirical modeling approaches, *Remote Sens. Environ.*, *114*(5), 1053–1068.
Preti, F., A. Dani, and F. Laio (2010), Root profile assessment by means of hydrological, pedological and above-ground vegetation information for bio-engineering purposes, *Ecol. Eng.*, *36*(3), 305–316.
Price, K., C. R. Jackson, A. J. Parker, T. Reitan, J. Dowd, and M. Cyterski (2011), Effects of watershed land use and geomorphology on stream low flows during severe drought conditions in the southern Blue Ridge Mountains, Georgia and North Carolina, United States, *Water Resour. Res.*, *47*, W02516, doi:10.1029/2010WR009340.
Roering, J. J., K. M. Schmidt, J. D. Stock, W. E. Dietrich, and D. R. Montgomery (2003), Shallow landsliding, root reinforcement, and the spatial distribution of trees in the Oregon Coast Range, *Can. Geotech. J.*, *40*(2), 237–253.
Running, S. W., and E. R. Hunt (1993), Generalization of a forest ecosystem process model for other biomes, BIOME-BCG, and an application for global-scale models, in *Scaling Physiological Processes: Leaf to Globe*, edited by J. R. Ehleringer and C. B. Field, pp. 141–158, Academic Press Inc., San Diego, Calif.
Running, S. W., R. R. Nemani, and R. D. Hungerford (1987), Extrapolation of synoptic meteorological data in mountainous terrain and its use for simulating forest evapotranspiration and photosynthesis, *Can. J. For. Res.*, *17*(6), 472–483.
Ryan, M. G., D. Binkley, J. H. Fownes, C. P. Giardina, and R. S. Senock (2004), An experimental test of the causes of forest growth decline with stand age, *Ecol. Monogr.*, *74*(3), 393–414.
Sakals, M. E., and R. C. Sidle (2004), A spatial and temporal model of root cohesion in forest soils, *Can. J. For. Res.*, *34*(4), 950–958.
Schenk, H. J., and R. B. Jackson (2002), The global biogeography of roots, *Ecol. Monogr.*, *72*(3), 311–328.
Schwarz, M., D. Cohen, and D. Or (2010), Root-soil mechanical interactions during pullout and failure of root bundles, *J. Geophys. Res.*, *115*, F04035, doi:10.1029/2009JF001603.
Seager, R., A. Tzanova, and J. Nakamura (2009), Drought in the southeastern United States: Causes, variability over the last millennium, and the potential for future hydroclimate change, *J. Clim.*, *22*(19), 5021–5045.
Sellers, P. J. (1985), Canopy reflectance, photosynthesis and transpiration, *Int. J. Remote Sens.*, *6*(8), 1335–1372.
Song, C., C. E. Woodcock, K. C. Seto, M. P. Lenney, and S. A. Macomber (2001), Classification and change detection using Landsat TM data: When and how to correct atmospheric effects?, *Remote Sens. Environ.*, *75*(2), 230–244.
Song, C., M. B. Dickinson, L. Su, S. Zhang, and D. Yaussey (2010), Estimating average tree crown size using spatial information from Ikonos and QuickBird images: Across-sensor and across-site comparisons, *Remote Sens. Environ.*, *114*(5), 1099–1107.
Tague, C. L., and L. E. Band (2004), RHESSys: Regional Hydro-Ecologic Simulation System—An object-oriented approach to spatially distributed modeling of carbon, water, and nutrient cycling, *Earth Interact.*, *8*(1), 1–42, doi:10.1175/1087-3562(2004)8<1:RRHSSO>2.0.CO;2.
Tucker, C. J. (1979), Red and photographic infrared linear combinations for monitoring vegetation, *Remote Sens. Environ.*, *8*(2), 127–150.
Turner, T. R., S. D. Duke, B. R. Fransen, M. L. Reiter, A. J. Kroll, J. W. Ward, J. L. Bach, T. E. Justice, and R. E. Bilby (2010), Landslide densities associated with rainfall, stand age, and topography on forested landscapes, southwestern Washington, USA, *For. Ecol. Manage.*, *259*(12), 2233–2247.
Vieilledent, G., B. Courbaud, G. Kunstler, J.-F. Dhote, and J. S. Clark (2010), Individual variability in tree allometry determines light resource allocation in forest ecosystems: A hierarchical Bayesian approach, *Oecologia*, *163*(3), 759–773.
White, P. S. (1979), Pattern, process, and natural disturbance in vegetation, *Bot. Rev.*, *45*(3), 229–299.
Wooten, R. M., R. S. Latham, A. C. Witt, S. J. Fuemmeler, and J. C. Reid (2007), Landslide hazards and landslide hazard mapping in North Carolina, paper presented at 1st North American Landslide Conference, Assoc. of Environ. and Eng. Geol., Vail, Colo.
Wu, T. (1995), Slope stabilization 7, in *Slope Stabilization and Erosion Control: A Bioengineering Approach*, vol. 233, edited by R. P. C. Morgan and R. J. Rickson, pp. 221–264, E&FN Spon/Chapman and Hall, London.
Wu, T. H., W. P. McKinnell Iii, and D. N. Swanston (1979), Strength of tree roots and landslides on Prince of Wales Island, Alaska, *Can. Geotech. J.*, *16*(1), 19–33.
Zheng, D. L., J. Rademacher, J. Q. Chen, T. Crow, M. Bresee, J. le Moine, and S. R. Ryu (2004), Estimating aboveground biomass using Landsat 7 ETM+ data across a managed landscape in northern Wisconsin, USA, *Remote Sens. Environ.*, *93*(3), 402–411.
Zhu, A., L. Band, R. Vertessy, and B. Dutton (1997), Derivation of soil properties using a soil land inference model (SoLIM), *Soil Sci. Soc. Am. J.*, *61*(2), 523–533.